Effect of Rotational Mobility on Photoelectron Transfer: Comparison of Two Zeolite Topologies

Michael A. Coutant,[†] **Joseph R. Sachleben,**[‡] **and Prabir K. Dutta*,**[†]

Department of Chemistry, The Ohio State University, Columbus, Ohio 43210, and
Department of Chemistry, Otterbein College, Westerville, Ohio 43081

Received: January 12, 2003; In Final Form: June 16, 2003

Nuclear magnetic resonance (NMR) spectroscopy and time-resolved diffuse reflectance (TRDR) have been combined to study the effects of constrained rotational motion on the rates of photoinduced electron-transfer reactions within zeolites. By synthesizing tris(2,2′-bipyridine) ruthenium (II) [Ru(bpy)$_3^{2+}$] within the large cages of zeolites Y and EMT, it was possible to directly investigate the effect of zeolite cage size on molecular motion of Ru(bpy)$_3^{2+}$ and the influence of the cage size on the rate of intrazeolitic electron transfer. Deuterium solid-state NMR shows that zeolite Y imposes restraint on molecular rotation of Ru(bpy)$_3^{2+}$, while zeolite EMT allows for motion. Temperature-dependent studies show the ability to freeze or induce motion of Ru-(bpy)$_3^{2+}$ within zeolite EMT while motion within zeolite Y remains unaffected, even at elevated temperatures. For zeolite EMT, an increase in the rate of the photoinduced forward and back electron transfer from Ru-(bpy)$_3^{2+}$ to methyl viologen was noted and correlated with access, rotational motion, and favorable orbital overlap. The overall photochemical charge separation efficiencies for the intrazeolitic Ru(bpy)$_3^{2+}$-bipyridinium reactions were similar for both zeolites.

Introduction

One of the major obstacles in the development of artificial photosynthetic systems is that the thermal back-electron transfer reaction negates the utilization of photochemically created reactive redox species.[1] Thus, considerable effort is being made to understand the features that control electron-transfer dynamics. Toward that end, many donor−acceptor systems have been examined, and assembly of molecular units on microheterogeneous supports is being pursued to influence electron-transfer dynamics.[2] By virtue of the nature of microheterogeneous supports, the motion of molecules is modified and it is of interest to examine how electron transfer is influenced by such immobilization. Zeolites, because of the molecular size of their cavities, are an excellent host system to investigate immobilization phenomena.

Zeolite Y consists of a regular network of sodalite cages in a tetrahedral arrangement resulting in 13 Å supercages with 7 Å windows (Figure 1a).[3] This is large enough to accommodate the luminescent molecule trisbipyridine ruthenium (II) [Ru-(bpy)$_3^{2+}$] which has a molecular diameter of 12 Å and can be assembled within the supercages by using a "ship-in-a-bottle" synthetic procedure.[4] These intrazeolitic ruthenium complexes can then be surrounded by bipyridinium ions such as methyl viologen (MV^{2+}) using the inherent ion-exchange properties of the zeolite. It has been shown that zeolite Y can promote long-lived, Ru(bpy)$_3^{3+}$−bipyridinium radical cation charge-separated states.[5,6] Molecular modeling of Ru(bpy)$_3^{2+}$ entrapped within zeolite Y indicated a significant number of contacts between the metal complex and the walls of the zeolite that were within the van der Waals radii of the atoms.[6] It was proposed that these contacts inhibit the rotational motion of the intrazeolitic Ru-(bpy)$_3^{2+}$, reducing the orbital overlap between donor and acceptor and the rate of back-electron transfer.[6]
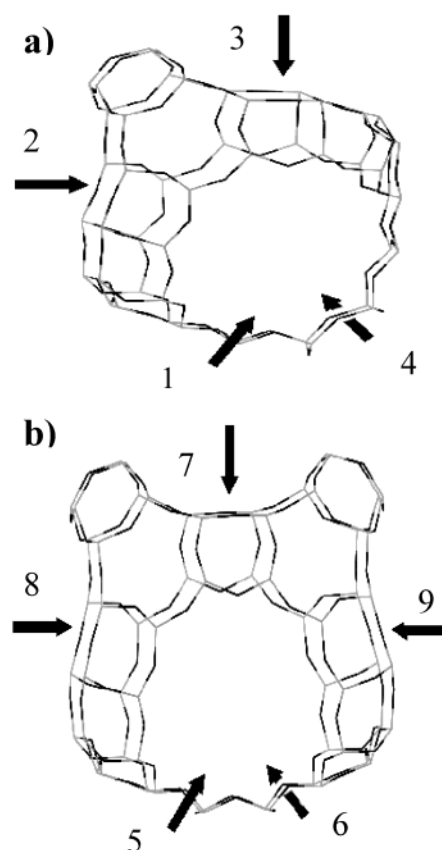

Figure 1. Models of the (a) supercage of zeolite Y and (b) hypercage of zeolite EMT. Arrows 1−4 point to the four 7.0 Å windows associated with equivalent supercages in zeolite Y. Arrows 5−7 point to 6.9 Å × 7.4 Å windows connected to adjacent hypocages. In EMT, arrows 8 and 9 point to two circular 7.4 Å windows that connect with neighboring hypercages.

To test the hypothesis that the constraint of motion by the zeolite cage affects the dynamics of electron transfer, we have

* To whom correspondence should be addressed. E-mail: dutta.1@osu.edu.
† The Ohio State University.
‡ Otterbein College.

Comparison of Two Zeolite Topologies

J. Phys. Chem. B, Vol. 107, No. 40, 2003 **11001**

examined in this paper a zeolitic environment where molecular motion is less inhibited than zeolite Y. To this end, we have performed the first known synthesis of $Ru(bpy)_3^{2+}$ within zeolite EMT. There are two kinds of large cages within zeolite EMT, a larger cage (hypercage) with dimensions of 13 Å × 14 Å with three 6.9 Å × 7.4 Å windows and two circular 7.4 Å windows (Figure 1b).[7] There is also a smaller cage (hypocage) of 12 Å in size with three 6.9 Å × 7.4 Å windows. These cages are present in equal ratios with two of each cage structure within a unit cell.

The motion of $Ru(bpy)_3^{2+}$ within zeolites Y and EMT was studied by ^2H solid-state nuclear magnetic resonance (NMR) spectroscopy. Though there are several reports using this technique to study molecules in zeolite hosts,[8a-e] the present study is the first attempt to study entrapped species as a function of cage size. Static molecules give a broad pattern typical of a powder (Pake pattern), whereas rotating molecules yield a single narrow peak. The narrowing of the signal is due to the time averaging of the signals from different molecular orientations as isotropic motion of the sample is induced. We have used time-resolved and steady-state spectroscopies to correlate rates of electron transfer and charge separation efficiency with the degree of $Ru(bpy)_3^{2+}$ rotational motion determined by NMR.

Experimental Section

Synthesis of Zeolite EMT. Synthesis of zeolite EMT was adapted from the literature.[7a] In a beaker, 1.82 g of sodium aluminate (Chem Service), 1.87 g of 50/50 w/w aqueous sodium hydroxide (Mallinckrodt), 1.84 g of 18-crown-6 (Aldrich), and 12.11 g of distilled water were stirred for 24 h. To this mixture was added 12.5 g of Ludox HS-40 colloidal silica (Aldrich), and it was mixed for 48 h at which point the resulting gel (final composition, 1 18-crown-6: 2.4 Na_2O: 1 Al_2O_3: 10 SiO_2: 140 H_2O) was placed in a Teflon-lined autoclave (Parr Instrument Company) at 110° C for 10 days.

Synthesis of Intrazeolitic $Ru(bpy)_3^{2+}$. The synthesis and purification of zeolite entrapped $Ru(bpy)_3^{2+}$ has been described in previous work with slight modifications made for zeolite EMT.[4] [$Ru(NH_3)_6^{3+}$] was ion exchanged with zeolite EMT for 2 days. The exchanged sample was dried and suspended in a 0.006 M bipyridine solution in ethanol. The ethanol was evaporated under nitrogen and the remaining powder was slowly heated under vacuum raising the temperature 25 °C every hour until a final temperature of 200 °C was achieved and maintained under vacuum for 24 h. Deuterium labeled samples were prepared in a similar manner, except that deuterium labeled bipyridine-d_8 (CDN isotopes) was utilized after the $Ru(NH_3)_6^{3+}$ exchange. The loading levels of $Ru(bpy)_3^{2+}$ were 1 per 30 cages for zeolite EMT and 1 per 30 supercages for zeolite Y.

Zeolite Characterization. X-ray powder diffraction (XRD) spectroscopy was performed with a Rigaku Geigerflex diffractometer using Ni-filtered Cu Kα radiation (40 kV and 25 mA). Scanning electron microscopy (SEM) studies were performed on a JEOL JSM-820 scanning electron microscope. Si/Al of the zeolite samples was obtained with a Bruker DMX 400 NMR spectrometer. Surface area measurements were performed with a Micromeritics Pulse Chemisorb 2700.

Steady-State Luminescence Spectroscopy. Emission spectra were measured using a Spex Fluorolog fluorometer. All emission spectra were corrected for the lamp emission profile. To achieve temperature variation, an Oxford DN1704 liquid nitrogen cryostat with ITC 502 intelligent temperature controller was used.

Time-Resolved Luminescence Measurements. Fluorescence lifetimes were measured using a Quantel YG581 Nd:YAG 15

ns pulsed at 1 Hz. The fluorescence was analyzed using a single monochromator (Acton Research Corporation model 265) set at 620 nm and a photomultiplier. The PMT signal was sent to a Tektronix DSA 601 digitizing analyzer oscilloscope where 256 decays were collected and averaged. Emission decays were fit using the Albery model.

UV−Vis Diffuse Reflectance Measurements. UV−vis diffuse reflectance spectra were obtained using a Shimadzu UV-265 spectrometer with a HVC-DRP reflective attachment, built by Harrick Scientific.

Solid-State ^2H NMR Spectroscopy. All NMR data were taken on a Bruker DMX 400 NMR spectrometer operating at a ^2H frequency of 61.4 MHz and a ^{29}Si frequency of 79.46 MHz. ^{29}Si spectra were taken with standard 1 pulse experiments using full 90° pulses and waiting 5 min between scans. Spectra were referenced externally to tetramethylsilane. Deuterated water (99.9%) was used as an external ^2H reference and also to calibrate the deuterium pulse strengths. Deuterium 90-degree times were measured to be 2.75 μs. All free induction decays of intercalated compounds were taken with 512 complex points over a sweep width of 500 kHz. The FID was apodized with 1 kHz of Gaussian line broadening, zero filled to 1 K complex data points, and Fourier transformed. MAS spectra were acquired at a spinning frequency of 14.5 kHz. Static and MAS spectra were taken using a quad echo sequence to remove the effects of probe ringing. The quad echo was not synchronized with the rotor period of the MAS because of the loss of signal due to T_2 effects. For this reason, large first-order phase shifts and baseline correction were necessary on the MAS spectra. Temperature of the sample in the MAS probe were calibrated by utilizing the chemical shift of $Pb(NO_3)_2$.[9a] Experimental data was compared to simulations obtained using the "dmfit program".[9b] Numbers for quadrupolar coupling constants were extracted using this simulation program.

Time-Resolved Diffuse Reflectance Spectroscopy. The TRDR setup has been previously described.[6] Excitation was provided by a Quantel Nd:YAG Q-switched laser with a 15 ns pulse width pulsed at 1 Hz. A 250 W pulsed Xenon arc lamp (Applied Physics) was used as the probe. The timing of the laser and lamp pulse, time delay, and detection window (100 ns) was done with an EG&G high voltage pulse generator and a timing box for triggering of the Q-switch and lamp pulse.

Steady-State Photolysis. The light source was a xenon-arc lamp (model A1010, 150−200 W) equipped with a water filter and a mirror that reflects radiation in the range of 420−650 nm (250 mW/cm²). A total of 50 mg of $Ru(bpy)_3^{2+}$−zeolite was exchanged twice with a 0.1 M solution of N,N'-tetramethylene-2,2'-bipyridinium dibromide (4DQBr₂) for 24 h. A total of 10 mg of the zeolite sample and 10 mg of propyl viologen sulfonate (PVS) were placed in an NMR tube with a micro spinning bar, and evacuated for several hours at 10^{-4} Torr. Degassed water was distilled over, and the suspension was freeze−pump−thawed three times. The tube was sealed and photolyzed, and the growth of the $PVS^{\bullet-}$ solution was monitored with a Shimadzu UV-2501 PC UV−vis spectrophotometer.

Kinetic Modeling of TRDR Data. Modeling of the decay of the bipyridinium radical from TRDR measurements was done by using STELLA, a system dynamics modeling software from High Performance Systems, Inc., Hanover, NH.[6]

Molecular Modeling. Molecular models of zeolites, $Ru(bpy)_3^{2+}$, and the methyl viologen ions were generated using published crystallographic data[3,10] on an IBM RISC System/600 computer, with the program Cerius (BIOSYM/Molecular Simulation).
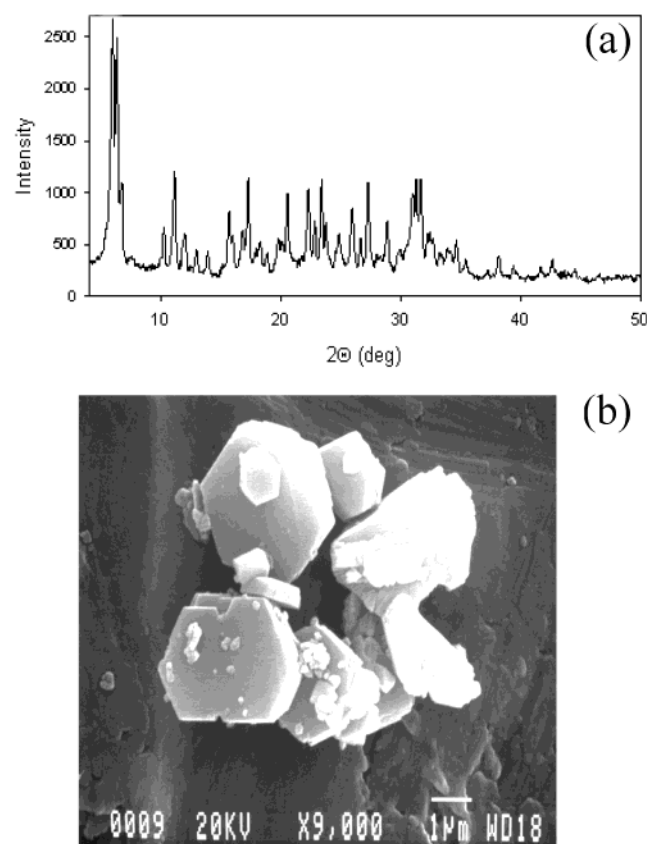
Figure 2. (a) X-ray diffraction (XRD) pattern and (b) scanning electron microscope image for synthesized zeolite EMT.

Figure 3. Emission spectra of Ru−Y and Ru−EMT taken at 77 K. Excitation wavelength- 450 nm, loading level 1 Ru(bpy)$_3^{2+}$ per 30 large cages for zeolite Y and EMT (both hyper and hypocages included).

Results

I. Synthesis and Characterization. Figure 2a shows the powder diffraction pattern of calcined EMT and is comparable to published data.[7c] Information about phase purity can be obtained from the diffraction data.[7d] The only anomaly that can be seen in Figure 2a is the increase in intensity of the peak at $2\theta = 12.5°$, which could be due to gmelinite.[7d] Interestingly, this peak is not observed in as-prepared samples and appears only after calcination. Considering the low intensity of the impurity peak, the EMT sample under study is relatively phase-pure. Figure 2b shows the scanning electron micrographs of the EMT sample, with the characteristic hexagonal plate-morphology.[7a] Small particles (smaller than 100 nm) and aggregates are also observed in the micrographs and could be the gmelinite phase. The ^{29}Si solid-state NMR gave a framework Si/Al ratio of 4.1, and the surface area measured by BET method was of 587 m²/g, typical of an open framework zeolite.

Our aim was to synthesize the ruthenium complex exclusively within the larger hypercage of EMT (13 Å × 14 Å). Also of concern would be partial synthesis resulting in the mono or bis complexes [Ru(bpy)(H$_2$O)$_4^{2+}$, Ru(bpy)$_2$(H$_2$O)$_2^{2+}$], especially within the smaller cages. To ensure that Ru(bpy)$_3^{2+}$ was exclusively synthesized within the larger cages, longer exchange times and a slow ramping in temperature during the heating step were employed. We reasoned that this process should allow the migration into the hypercages, where the larger cage size should make the formation of the trisbipyridyl complex more favorable. Loading levels were kept low, with a final concentration of 1 Ru(bpy)$_3^{2+}$ per 30 cages (includes both hyper and hypocages). Identical synthesis conditions were also chosen for Ru(bpy)$_3^{2+}$ in zeolite Y, and thus, the loading levels are comparable for both frameworks. Upon dissolving the EMT
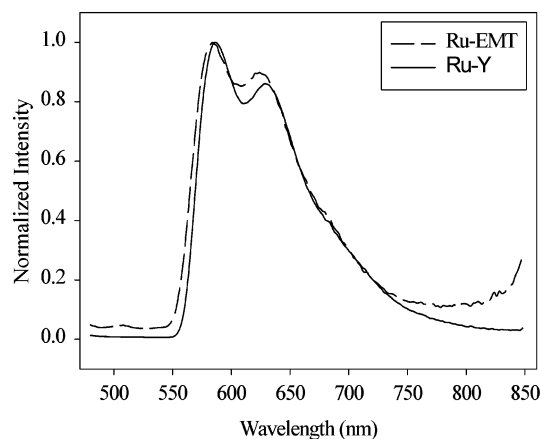
zeolite in HF, the extracted solution had identical absorption and emission profiles compared to a stock solution of Ru-(bpy)$_3^{2+}$(aq). Ru(bpy)$_2$(H$_2$O)$_2^{2+}$ absorbs between 480 and 490 nm and exhibits no emission at room temperature.[11] The lack of absorption in the region of 480−490 nm and high degree of luminescence indicated no formation of the bis complex. Calzaferri and co-workers have shown that in zeolite Y, the loading level of Ru(bpy)$_3^{2+}$ is determined by the diffusion of bipyridine ligand, which gets restricted at the higher loading levels (2 complexes per 3 supercages), and it is of interest to examine if the larger hypercages in EMT can lead to higher loadings.[12]

The UV−vis diffuse reflectance and luminescence spectra of Ru(bpy)$_3^{2+}$−EMT, abbreviated as Ru−EMT, showed the characteristic MLCT and $\pi-\pi^*$ bipyridine bands at 450 and 280 nm and a fluorescence band at 620 nm typical of Ru(bpy)$_3^{2+}$ in solution and zeolite Y.[4] The emission spectra at 77 K in both zeolites consisted of similar line shapes; however, the spectrum for Ru−EMT is blue-shifted by 5 nm (Figure 3).

The major difference between the two zeolites was in the luminescent lifetime of Ru(bpy)$_3^{2+}$. For the complex entrapped within EMT, the lifetime was ∼450 ns as compared to ∼600 ns in zeolite Y. Temperature-dependent lifetime measurements were made, and the decay profiles fitted with the equation

$$\tau^{-1}(t) = k_1 + k_2 e^{-\Delta E_1/kT} + k_3 e^{-\Delta E_2/kT} \qquad (1)$$

as has been done for zeolite Y,[4c,13] where $\tau(t)$ is the temperature-dependent lifetime, k_1, k_2, and k_3 are rate constants, and ΔE is an energy difference term. In this equation, k_1 represents the sum of radiative (k_r) and nonradiative rate (k_{nr}) constants representing decay from a series of three excited states in thermal equilibrium. The temperature dependent terms account for two thermally accessible excited states ΔE_1 and ΔE_2 above the first excited state with rate constants k_2 ($k_r + k_{nr}$) and k_3 ($k_r + k_{nr}$). The excited state and decay pathways of Ru(bpy)$_3^{2+}$ are well characterized.[14] The three lowest ^{3}MLCT states from which both radiative and nonradiative decay occurs are in thermal equilibrium. A fourth ^{3}MLCT state exists ∼800 cm^{-1} in energy (ΔE_1) above the lowest ^{3}MLCT state. The second thermally accessible state is a metal-centered ^{3}dd state (∼3000 cm^{-1} above the lowest ^{3}MLCT states, ΔE_2) that is associated with ligand loss and photodegradation. The thermally accessible ^{3}dd state is characterized by an elongation of the Ru−N bond.[14c] It has been proposed that entrapment by a solid matrix increases the energy of this state by hindering elongation, and previous
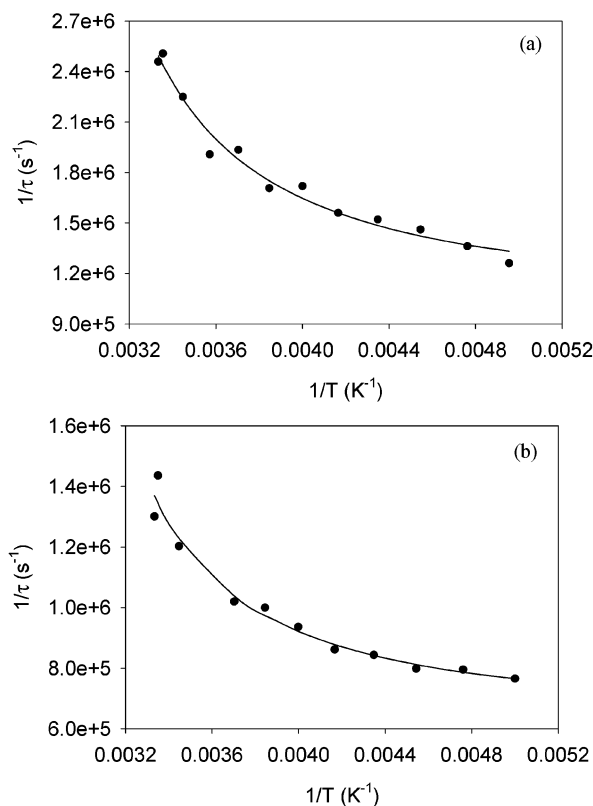
Comparison of Two Zeolite Topologies

J. Phys. Chem. B, Vol. 107, No. 40, 2003 **11003**

Figure 4. Dependence of the emission lifetimes of Ru(bpy)$_3^{2+}$ in Na–EMT (a) and TEA–EMT (b) on temperature. Solid lines are fit to the data using eq 1 (loading level 1 Ru(bpy)$_3^{2+}$ per 30 large cages, emission monitored at 620 nm).

studies have noted that decay from the ^{3}dd state is not seen within zeolite Y and other solid matrixes.[4c,15] In solution where there is no hindrance for bond elongation, the ^{3}dd state dominates the temperature dependence of the excited-state decay.[14a]

The excited-state decay pathways for sodium and tetraethyl-ammonium (TEA) exchanged Ru–EMT samples were investigated. TEA was chosen because it was known from previous studies[13] on zeolite Y that it altered the lifetime of encapsulated Ru(bpy)$_3^{2+}$ and provided an extra set of data points for ensuring that the excited-state parameters calculated from fitting of the lifetime data are consistent for EMT. Figure 4 shows the temperature-dependent measurements and fits for Ru–Na–EMT and Ru–TEA–EMT. The fitting parameters are listed in Table 1 and compared with the results from previous studies on zeolite Y and solution.[13,14a] The fit for the temperature-dependent lifetimes of the Ru–EMT required the use of both thermal deactivation pathways as compared to Ru–Y, where contributions from the ^{3}dd state was not necessary to be included.

II. Intrazeolitic Mobility of Ru(Bpy)$_3^{2+}$. Deuterated Ru-(bpy)$_3^{2+}$ was synthesized within the cages of zeolites Y and EMT using bipyridine ligands with all deuterium atoms (loading levels were 1 Ru(bpy)$_3^{2+}$ per 30 large cages for both zeolites).
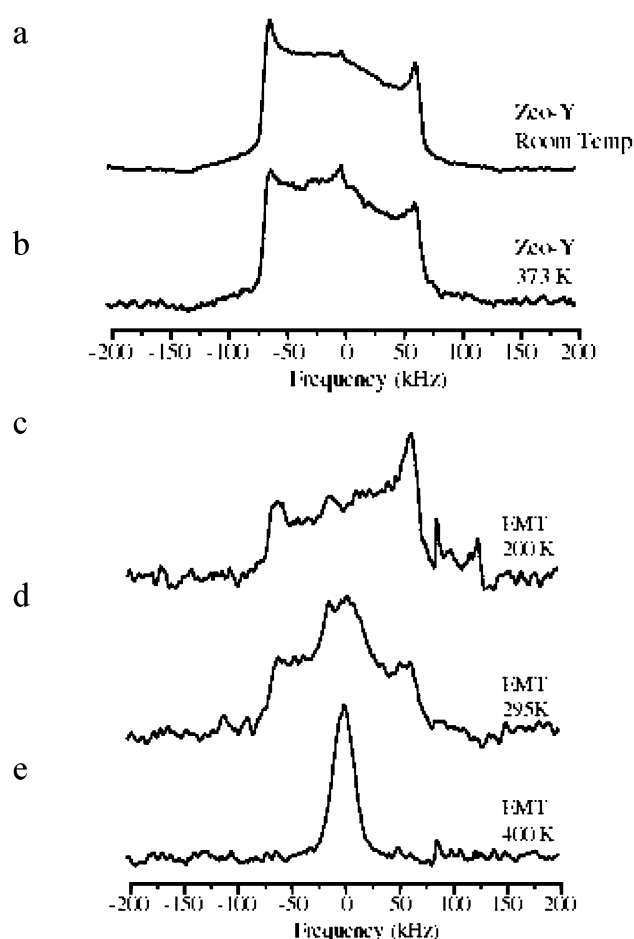

Figure 5. Temperature-dependent ^{2}H quad-echo solid-state NMR spectra of Ru–Y and Ru–EMT with deuterated bipyridine ligands (loading level 1 Ru(bpy)$_3^{2+}$ per 30 large cages in zeolites EMT and Y).

TABLE 2: Results of Kinetic Analysis of TRDR Decays

sample	k_f (s^{-1})	k_b (s^{-1})	k_{hop} (s^{-1})	k_2 (conc^{-1} s^{-1})
Ru–MV–Y	7.9×10^7	9.0×10^4	2.0×10^5	3.0×10^3
Ru–MV–EMT	1.7×10^8	3.2×10^5	2.0×10^5	3.0×10^3

Figure 5 shows the temperature-dependent ^{2}H NMR spectra of Ru–Y and Ru–EMT samples. With little-to-no motion present in Ru–Y, there was no need to attempt to freeze the motion at lower temperatures, so an attempt was made to induce motion by increasing the temperature. Studies at 373 K (Figure 5b) showed no narrowing of line shape with respect to the 295 K spectrum (Figure 5a), indicating that motion is not induced at this increased temperature. ^{2}H NMR studies of Ru–EMT at room temperature (Figure 5d) indicate a sample with slight rotational mobility. By lowering the temperature to 200 K, it is possible to freeze out the rotational motion of Ru(bpy)$_3^{2+}$ resulting in a powder spectrum (Figure 5c) similar to that of room-temperature Ru–Y (Figure 5b). At an increased temper-

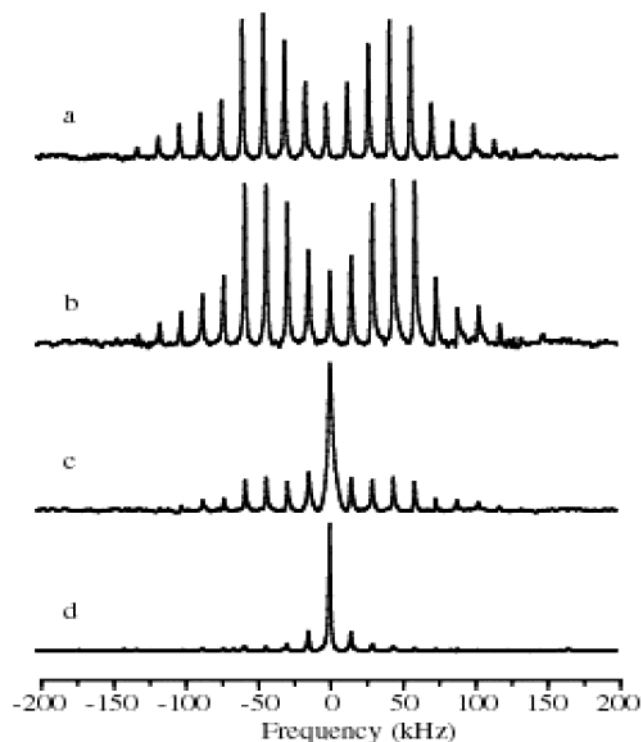**TABLE 1: Fits of Temperature-Dependent Lifetimes for Ru–EMT and Ru–Y**

sample	k_1 (s^{-1})	k_2 (s^{-1})	ΔE (cm^{-1})	k_3 (s^{-1})	ΔE (cm^{-1})	room temp. lifetime (ns)
Ru–Na–Y[a]	5.49×10^5	4.9×10^7	800	N/A	N/A	620
Ru–Na–EMT	1.19×10^6	4.4×10^7	800	6.35×10^{11}	3000	430
Ru–TEA–Y[a]	4.85×10^5	1.64×10^7	800	N/A	N/A	1220
Ru–TEA–EMT	6.98×10^5	2.1×10^7	800	3.86×10^{11}	3000	790
Ru(bpy)$_3^{2+}$ (aq)[b]	12.9×10^5	N/A	N/A	1.0×10^{13}	3560	630

[a] Taken from ref 6. [b] Taken from ref 14a.

Figure 6. ^{2}H MAS spectra of intrazeolitic deuterated Ru(bpy)$_3^{2+}$: (a) Spectrum of Ru−Y at 300 K, (b) Spectrum of Ru−EMT at 200 K, (c) Spectrum of Ru−EMT at 300 K, (d) Spectrum of Ru−EMT at 400 K (loading levels same as Figure 5).

ature of 400 K, enough mobility is imparted to give a single, narrow ^{2}H NMR signal indicative of isotropic motion (Figure 5e).

To quantify the effect of motion on the deuterium spectra, the MAS spectra shown in Figure 6 were simulated, and the values of the quadrupole coupling constant (QCC) were extracted. The values of the quadrupole coupling constant (QCC) are often reported as a measure of motion because its value depends on the value of the electric field gradient:

$$QCC = (e^2 q_{zz} Q)/h \qquad (2)$$

where e is the charge of the electron, q_{zz} as the largest component of the electric field gradient, Q is the nuclear electric quadrupole moment, and h is Planck's constant.[8] As molecules begin to rotate in the large external magnetic field, q_{zz} averages out, reducing the magnitude of QCC. For Ru−Y at 300 K (Figure 6a), the value of QCC is 172 kHz which is close to that of a sample of static benzene (190 kHz).[8c] ^{2}H MAS studies of Ru−EMT at 300 K (Figure 6c) indicate a sample with slight rotational mobility. By lowering the temperature to 200 K, it is possible to freeze out the rotational motion of Ru(bpy)$_3^{2+}$ (QCC = 172 kHz) resulting in an MAS sideband pattern (Figure 6b) indistinguishable from that of room-temperature Ru−Y (Figure 6a). At an increased temperature of 400 K (Figure 6d), the value of QCC is reduced to 30 kHz, showing that highly symmetrical and rapid motion of the molecule is occurring in the EMT cages. Two possibilities for the motion are rotational diffusion over a sphere or octahedral jumps, which, along with the rates of motion are subjects of future study.

III. Intrazeolitic Photoinduced Electron Transfer. *Forward Electron Transfer.* The forward electron-transfer rate between Ru(bpy)$_3^{2+}$ and methyl viologen within zeolite EMT was estimated from the emission data. Figure 7 shows the emission profile of Ru−EMT exchanged with different amounts of methyl
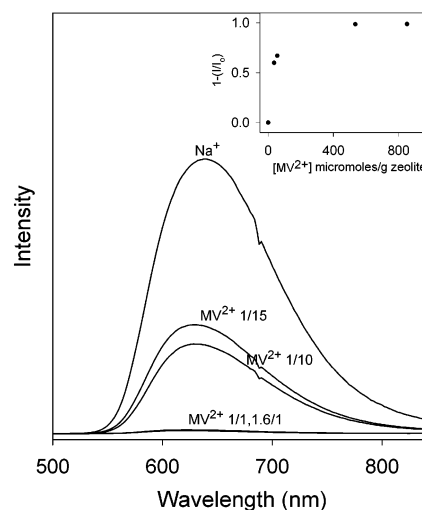

Figure 7. Quenching of the emission of Ru(bpy)$_3^{2+}$−EMT with increased loadings of MV^{2+}. The inset shows the emission intensity changes with intrazeolitic loading of MV^{2+}, loading levels are reported as molecule of bipyridinium ion per large cage, e.g., 1/15 refers to 1 MV^{2+} per 15 hyper and hypocages (excitation wavelength, 450 nm; loading level 1 Ru(bpy)$_3^{2+}$ per 30 large cages).

viologen ion. The inset shows a plot of the maximum intensity as a function of micromoles of MV^{2+} per gram of zeolite. From these data, a rate constant for the forward electron-transfer reaction was estimated using the re-organized Stern−Volmer equation under the assumption of static quenching.[16] This gives a value of 1.7×10^8 s^{-1}, a value higher by a factor of 2.2 than the value for Ru−Y (7.9×10^7 s^{-1}) observed for zeolite Y.[5]

Back Electron Transfer. The transient diffuse reflectance spectra of Ru−MV−Y and Ru−MV−EMT 100 ns after the laser pulse are shown in parts b and c of Figure 8, respectively. Both these spectra were obtained at a viologen loading of 1.5−1.7 molecules per supercage. In these spectra, there is a band at 389 nm appearing 100 ns after the laser pulse due to the presence of methyl viologen radical cation (MV$^{•+}$). The band at 370 nm due to Ru(bpy)$_3^{2+*}$ seen in the sample without MV^{2+} (Figure 8a) has disappeared in the viologen-exchanged samples due to the electron-transfer quenching of Ru(bpy)$_3^{2+*}$. Within the minimum time for which the detector gate is left open (100 ns), the transient signal of MV$^{•+}$ is maximized, confirming the earlier result that the rate of forward electron transfer is faster than 10^7 s^{-1}. The signal in the EMT sample is considerably weaker than the zeolite Y sample, and this is puzzling considering that the loading levels of Ru(bpy)$_3^{2+}$ are comparable. We do not have a good explanation for this effect, except to note that the morphologies of the zeolites are quite different, being spherical in case of zeolite Y and flat-plate like crystals for EMT. Such differences in morphology will alter the scattering properties of the radiation used in the diffuse reflectance experiments.

The kinetics of the back electron-transfer reaction between Ru(bpy)$_3^{3+}$ and MV$^{•+}$ can be obtained by monitoring the decay of the MV$^{•+}$ signal. Figure 9 shows the decay of the MV$^{•+}$ signal for Ru−EMT (the data for Ru−Y was comparable to the previous work[6]). The equations that model the electron transfer process within zeolites for a high loading of acceptor have been previously described and involve the back electron-transfer reaction (k_b), a hopping process (k_{hop}), and a recombination modeled as k_2, a second-order rate constant.[6] Using these equations, the decay of the MV$^{•+}$ was simulated for both Ru−Y and Ru−EMT and the data for Ru−EMT is shown as the solid line in Figure 9.
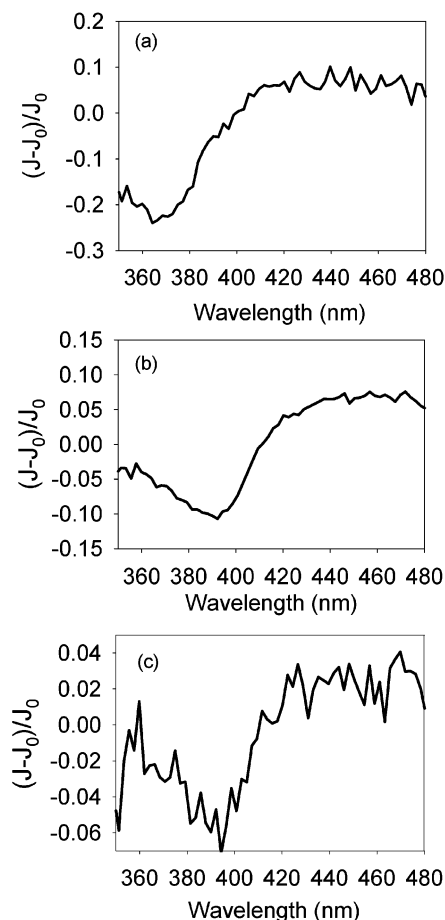
Figure 8. Comparison of TRDR spectra (100 ns after laser pulse) of (a) $Ru(bpy)_3^{2+}-Y$, (b) $Ru(bpy)_3^{2+}-MV^{2+}$ (1.7 per supercage)$-Y$, and (c) $Ru(bpy)_3^{2+}-MV^{2+}$ (1.5 per large cages)$-EMT$. Loading level 1 $Ru(bpy)_3^{2+}$ per 30 large cages in zeolites EMT and Y.

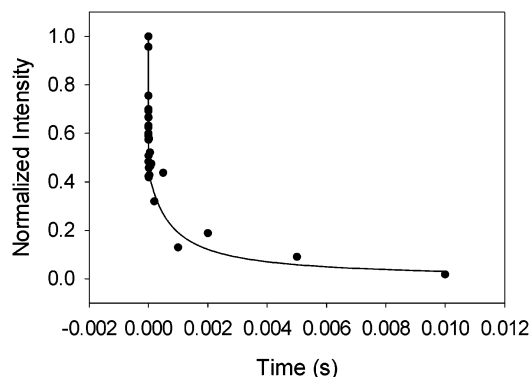**Figure 9.** Plot of the decay of methyl viologen radical cation signal for high loadings of methyl viologen (1.5 molecules per large cage) $Ru(bpy)_3^{2+}-$zeolite EMT. Solid lines are fits to the data using the model described in the chapter.

IV. Steady-State Photolysis. Steady-state photolysis was investigated to compare overall charge separation efficiencies. Ru−Y and Ru−EMT were ion exchanged with the electron acceptor *N,N′*-tetramethylene-2,2′-bipyridinium (4DQ^{2+}, 1.2 molecules/cage) and placed in a neutral propyl viologen sulfonate (PVS) solution. Through the hopping mechanism, charge can migrate to the surface and be transferred to the PVS in solution.[17] The resulting PVS radical anion can be monitored by UV−vis spectroscopy, and the data from zeolites Y and EMT are compared in Figure 10. Photolysis was carried out for 100

min, and within experimental error, the amount of PVS$^{-•}$ formed was comparable for zeolite EMT and Y.

Discussion

The loading levels of $Ru(bpy)_3^{2+}$ in both zeolites were of the order of 1 molecule per 30 large cages (for EMT, large cage is defined as both hypo- and hypercages) and so comparisons between the two frameworks can be made independent of the loading levels.

I. Influence of Zeolite Cage Size on Rotational Mobility of $Ru(bpy)_3^{2+}$. In the limit of a rigid lattice, each deuterium atom is associated with two transitions with frequencies dependent on the deuterium quadrupolar coupling constant and the orientation of the electric field gradient tensor (EFG) relative to the magnetic field.[8f,g] As a deuterium atom moves, its EFG experiences a range of possible sites. This results in line shapes dependent on the number of exchange sites, rate of exchange, and orientation of the EFG tensors for each site relative to the jump axis. With increasing isotropic motion, signals from different sites begin to average out, narrowing the resulting line shape. Thus, by measuring the powder line shapes, it is possible to extract information about molecular motion occurring in the regime between 10^3 and 10^8 per second (Hz). This time scale is convenient for monitoring motions affecting the forward and backward electron-transfer reactions examined in this report, which have rate constants of the order of 10^5-10^8 s^{-1}.

From the room temperature ^{2}H NMR spectra of Ru−EMT and Ru−Y, it is evident that $Ru(bpy)_3^{2+}$ experiences greater mobility within the hypercages of zeolite EMT. The line shape of Ru−EMT at room temperature indicate a rotational motion with the ruthenium complex possibly hopping between distinct sites. This motion can be modified to either the fast or slow motion extremes by altering the temperature of the measurement. Zeolite Y appears to impose considerable restraint upon the entrapped ruthenium complex, with increased temperatures unable to induce any appreciable motion on the time scale of the NMR experiment.

By designating a "bad" contact as one where two atoms approach each other at less than 90% of their van der Waals radii, it is possible to gain insight as to the constraints imposed by the zeolite framework (Figure 11). The model shows 14 "bad" contacts between the walls of the zeolite Y (mostly oxygen atoms) and the ruthenium complex (carbon and hydrogen atoms). For zeolite EMT, only one "bad" contact between $Ru(bpy)_3^{2+}$ and the walls of the zeolite framework was noticed. This modeling procedure depends on the manual manipulation of the different molecular orientations and cannot exhaustively examine all orientations of intrazeolitic $Ru(bpy)_3^{2+}$. However, it provides a good basis for comparing the two zeolites and is consistent with the NMR investigations of intrazeolitic mobility.

II. Influence of Mobility on Excited-State Properties of $Ru(bpy)_3^{2+}$. The electronic spectral properties of $Ru(bpy)_3^{2+}$ in zeolites Y and EMT are mostly comparable. The major difference is in the excited-state lifetimes of $Ru(bpy)_3^{2+}$, which differs by about 150 ns. The thermally accessible ^{3}dd state provides an efficient means of nonradiative decay and characterized by an elongation of the Ru−N bond.[14c] Experiments in solid matrixes including zeolite Y demonstrate that the steric constraints can hinder the Ru−N bond elongation, resulting in raising of the energy required for the ^{3}MLCT $\rightarrow$ ^{3}dd transition to the point where the ^{3}dd state is no longer thermally accessible.[4c] The resulting temperature dependence is then ascribed solely to transitions to the fourth ^{3}MLCT state (~800 cm^{-1}). A dramatic increase in excited-state lifetime (<10 ns to
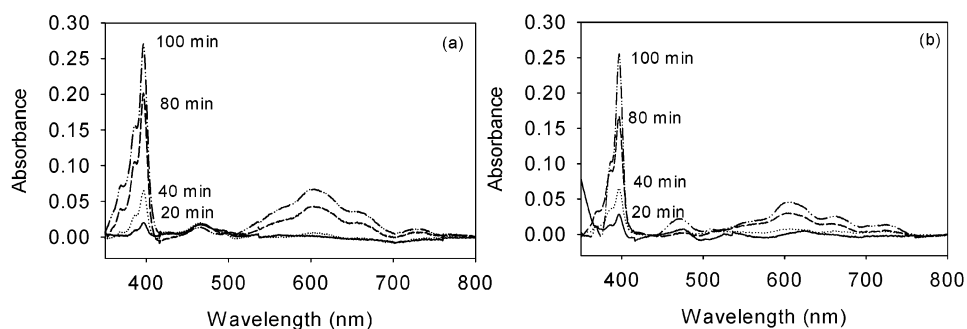
Figure 10. UV−vis spectra of the growth of PVS⁻• upon photolysis of (a) $Ru(bpy)_3^{2+}-4DQ^{2+}-Y$ and (b) $Ru(bpy)_3^{2+}-4DQ^{2+}-EMT$.
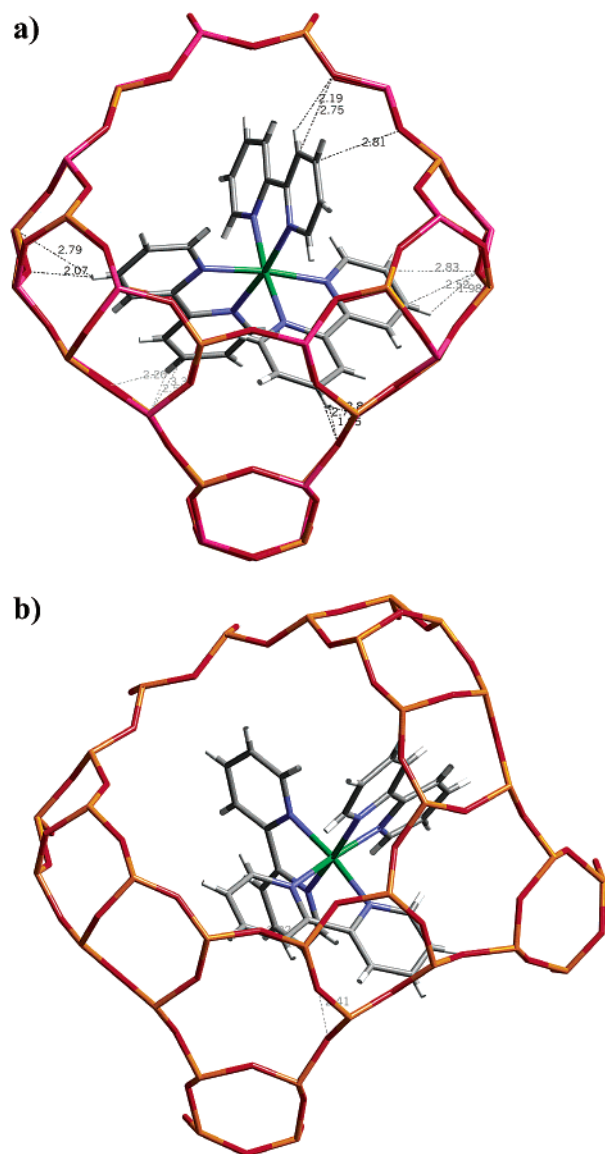

Figure 11. Computer models of $Ru(bpy)_3^{2+}$ within the supercage of zeolite Y (a) and the hypercage of zeoite EMT (b). Dotted lines indicate "bad" contacts between the zeolite and ruthenium complex.

302 ns) of a bis-heteroleptic, tris-ligated polypyridine complex of ruthenium (II) $[Ru(bpy)_2(daf)^{2+}$, daf = diazafluorene] upon entrapment within zeolite Y has been ascribed to the loss of the ^{3}dd as an effective means of excited-state deactivation.[18] Similarly, the excited-state lifetime of $Ru(bpy)_3^{2+}$ within a cellulose acetate matrix is 914 ns, an increase in 300 ns from aqueous measurements.[15,19] Zeolite EMT provides a less restrictive environment for $Ru(bpy)_3^{2+}$ as shown by the ^{2}H NMR

studies. The shorter lifetime of ambient Ru−EMT is ascribed to the availability of the ^{3}dd state and the temperature-dependent lifetime studies account for this by using two temperature-dependent terms. Temperature-dependent measurements of Ru−Y show the elimination of the ^{3}dd deactivation pathway within zeolite Y with an ambient lifetime of 600 ns.[6] This means that the intrazeolitic lifetime of $Ru(bpy)_3^{2+}$ is closer to ~500 ns upon zeolite encapsulation (as in EMT), and the highly constraining environment of zeolite Y then results in an increased excited-state lifetime due to the destabilization of the ^{3}dd state. It is known that the excited state of $Ru(bpy)_3^{2+}$ is sensitive to the surrounding environment.[14a,c,15] The zeolite is described as "superpolar",[20] and such an environment can account for the shorter lived excited-state lifetimes observed within the EMT zeolitic structure as compared to solution.

III. Influence of $Ru(bpy)_3^{2+}$ Mobility on Electron-transfer Dynamics. Comparison of the MV^{2+}-exchanged Ru−EMT and Ru−Y systems reveals a 2.2-fold increase in the forward electron-transfer rate constant for the EMT-based system. The increase in the forward electron-transfer reaction can be rationalized due to the differences between the structures of zeolite Y and EMT. The presence of five windows for the hypercage of zeolite EMT allows access to more MV^{2+} as compared to zeolite Y, which only has four windows. This increased access can provide for a more effective forward electron-transfer reaction.

The rate of back electron transfer, k_b, from $MV^{+•}$ to $Ru(bpy)_3^{3+}$ has increased by a factor of 3.5 upon switching from zeolite Y to EMT. The back-electron-transfer reaction needs to occur from the viologen radical to the $d\pi$ (A_1) orbital of the ruthenium atom that is in the center of the supercage.[21] The inability of $Ru(bpy)_3^{2+}$ to rotate in zeolite Y hinders favorable orbital overlap for the back-electron-transfer reaction,[6] slowing down the process, which is alleviated by the rotational motion of $Ru(bpy)_3^{2+}$ in EMT.

Previous work has demonstrated the importance of molecular orientation on electron transfer reactions. An early study involved picosecond fluorescent studies of porphyrins linked to quinones.[22] At low-temperatures (77 K), it was observed that the forward electron transfer rate constant had an angular dependence due to a frozen ensemble of rotational conformations. Another study involving a bisporphyrin separated by different molecular spacers altered the dihedral angle between donor and acceptor molecule. Electron transfer proceeded most efficiently at angles of 0° and 90° and was least efficient at a dihedral angle of 50°.[23] Wang et al. examined the dependence of electron transfer on rotational motion for an asymmetric carboxylic acid dendrimer with a single ferrocene postioned "off-center" in the dendrimer structure.[24] At a neutral pH, the surface of the dendrimer is highly negative and favors an orientation with the ferrocene pointed away from the electrode

Comparison of Two Zeolite Topologies

J. Phys. Chem. B, Vol. 107, No. 40, 2003 **11007**

surface. This interaction slowed the rotational reorientation of the dendrimer and consequently the rate of electron transfer.

Upon changing from Ru−Y to Ru−EMT, the rate constant for forward electron transfer from $Ru(bpy)_3^{2+}$ to MV^{2+} increases by 2.2, whereas the rate constant for the back electron transfer reaction increases by 3.5. A faster forward electron transfer reaction compensates for the correspondingly increased rate of back electron-transfer resulting in a minimal difference in the steady-state generation of PVS radical for zeolites Y and EMT, indicating that the overall charge separation efficiencies are comparable.

Conclusions

$Ru(bpy)_3^{2+}$ has been synthesized for the first time within the hypercages of zeolite EMT. These cages are lager than the supercage of zeolite Y, resulting in differences in excited-state decay and electron-transfer properties. Differences in the amount of rotational motion afforded by the different zeolite cages were investigated with ^2H solid-state NMR spectroscopy. When entrapped within zeolite Y, $Ru(bpy)_3^{2+}$ has little rotational mobility even at increased temperatures. However, within zeolite EMT there is motion at room temperature that can be increased further to a rapid isotropic motion with temperature. Changing the nature of the zeolitic environment also influenced the excited state and photoinduced electron-transfer properties of $Ru(bpy)_3^{2+}$. The luminescent lifetime is shorter in EMT due to the access of the thermally accessible ^3dd state. Both forward and back electron-transfer reactions were faster within zeolite EMT as compared to zeolite Y. This was also ascribed to the increased motion of $Ru(bpy)_3^{2+}$ molecules being able to reorient and provide access to the orbitals involved in the reaction. Comparable increases in forward and back electron transfer reactions resulted in only small differences in charge separation efficiency for steady-state photolysis in both zeolites.

References and Notes

(1) Bard, A. J.; Fox, M. A. *Acc. Chem. Res.* **1995**, *28*, 141.

(2) Vaidyalingam, A. S.; Coutant, M. A.; Dutta, P. K. *Electron-transfer processes in zeolites and related microheterogeneous media*; Balzani, V., Ed.; Wiley-VCH: Weinheim, Germany, 2001; Vol. 4, p 412.

(3) Olson, D. H. *J. Phys. Chem.* **1970**, *74*, 2758.

(4) (a) DeWilde, W.; Peeters, G.; Lunsford, J. H. *J. Phys. Chem.* **1980**, *84*, 2306. (b) Incavo, J. A.; Dutta, P. K. *J. Phys. Chem.* **1990**, *94*, 3075. (c)

Maruszweski, K.; Strommen, D. P.; Kincaid, J. R. *J. Am. Chem. Soc.* **1993**, *115*, 8345.

(5) Yonemoto, E. H.; Kim, Y. I.; Shcmehl, R. H.; Wallin, J. O.; Shoulder, B. A.; Richardson, B. R.; Haw, J. F.; Mallouk, T. E. *J. Am. Chem. Soc.* **1994**, *116*, 10557.

(6) Vitale, M.; Castagnola, N. B.; Ortins, N. J.; Brooke, J. A.; Vaidyalingam, A.; Dutta, P. K. *J. Phys. Chem. B* **1999**, *103*, 2408.

(7) (a) Burkett, S. L.; Davis, M. E. *Microporous Materials* **1993**, *1*, 265. (b) Su, B.-L.; Norberg, V.; Martens, J. A. *Microporous and Mesosporous Materials* **1998**, *25*, 151. (c) Baerlocher, C.; McCusker, L. B.; Chiappetta, R. *Microp. Mater.* **1994**, *2*, 269. (d) Wendelobo, R.; Stocker, M.; Junnggreen, H.; Mostad, H. B.; Akporiaye, D. E. *Microporous Mesosporous Mater.* **1999**, *28*, 361.

(8) (a) Auerbach, S. M.; Bull, L. M.; Henson, N. J.; Metiu, H. I.; Cheetham, A. K. *J. Phys. Chem.* **1996**, *100*, 5923. (b) Stepanov, A. G.; Shubin, A. A.; Luzgin, M.; Jobic, H.; Tuel, A. *J. Phys. Chem. B* **1998**, *102*, 10860. (c) Sato, T.; Kunimori, K.; Hayashi, S. *Phys. Chem. Chem. Phys.* **1999**, *1*, 3839. (d) Overweg, A. R.; Koller, H.; de Haan, J. W.; van de Ven, L. J. M.; van der Kraan, A. M.; van Santen, R. A. *J. Phys. Chem. B* **1999**, *103*, 4298. (e) Alexander, P. Gladden, L. F. *Zeolites,* **1997**, *18*, 38. (f) Schmidt, C.; Wefing, S.; Blumich, B.; Spiess, H. W. *Chem. Phys. Lett.* **1986**, *103*, 84. (g) Heaton, N. J.; Vold, R., R.; Vold, R. L. *J. Chem. Phys.* **1989**, *91*, 56.

(9) (a) Bielecki, A. Burum, D. P. *J. Magn. Reson.* **1995**, *A 116*, 215. (b) Massiot, D.; Fayon, F.; Capron, M.; King, I.; Le Calve, S.; Alonso, B.; Durand, J.-O.; Bujoli, B.; Gan, Z.; Hoatson, G. *Magn. Reson. Chem.* **2002**, *40*, 70.

(10) Rillema, D. P.; Jones, D. S.; Woods, C.; Levy, H. A. *Inorg. Chem.* **1992**, *31*, 935.

(11) (a) Durham, B.; Wilson, S. R.; Hodgson, D. J.; Meyer, T. J. *J. Am. Chem. Soc.* **1980**, *102*, 600. (b) Dutta, P. K.; Das, S. K. *J. Am. Chem. Soc.* **1997**, *119*, 4311.

(12) Laine, P.; Lanz, M.; Calzaferri, G. *Inorg. Chem.* **1996**, *35*, 3514.

(13) Coutant, M. A.; Le, T.; Castagnola, N.; Dutta, P. K. *J. Phys. Chem. B* **2000**, *104*, 10783.

(14) (a) Caspar, J. V.; Meyer, T. J. *J. Am. Chem. Soc.* **1983**, *105*, 5583. (b) Yersin, H.; Gallhuber, E.; Voglet, A.; Kunkely, H. *J. Am. Chem. Soc.* **1983**, *105*, 4155. (c) Meyer, T. J. *Pure Appl. Chem* **1986**, *58*, 1193.

(15) Allsopp, S. R.; Cox, A.; Kemp, T. J.; Reed, W. J. *J. Chem. Soc., Faraday Trans. 1* **1978**, *79*, 1275.

(16) Turro, N. J. *Modern Molecular Photochemistry*; The Benjamin/ Cummings Publishing Company, Inc.: Menlo Park, CA, 1978.

(17) (a) Borja, M.; Dutta, P. K. *Nature* **1993**, *362*, 43. (b) Sykora, M.; Kincaid, J. R. *Nature* **1997**, *387*, 162. (c) Castagnola, N. B.; Dutta, P. K. *J. Phys. Chem. B* **1998**, *102*, 1696.

(18) Maruszewski, K.; Kincaid, J. R. *Iong. Chem.* **1995**, *34*, 2002.

(19) Lumpkin, R. S.; Kober, E. M.; Worl, L. A.; Murtaza, Z.; Meyer, T. J. *J. Phys. Chem.* **1990**, *94*, 239.

(20) Uppili, S.; Thomas, J. K.; Crompton, E. M.; Ramamurthy, V. *Langmuir* **2000**, *16*, 265.

(21) Sun, H.; Yoshimura, A.; Hoffman, M. Z. *J. Phys. Chem.* **1994**, *98*, 5058.

(22) Leland, B. A.; Joran, A. D.; Felker, P. M.; Hopfield, J. J.; Zewail, A. H.; Dervan, P. B. *J. Phys. Chem.* **1985**, *89*, 5571.

(23) Helms, A.; Heiler, D.; McLendon, G. *J. Am. Chem. Soc.* **1991**, *113*, 4325.

(24) Wang, Y.; Cardona, C. M.; Kaider, A. E. *J. Am. Chem. Soc.* **1999**, *121*, 9756.